



# Reactions of ethanol over CeO<sub>2</sub> and Ru/CeO<sub>2</sub> catalysts



K. Mudiyansele<sup>a</sup>, I. Al-Shankiti<sup>a</sup>, A. Foulis<sup>c</sup>, J. Llorca<sup>b</sup>, H. Idriss<sup>a,\*</sup>

<sup>a</sup> Fundamental Catalysis, Centre for Research and Development (CRD), SABIC-KAUST, Thuwal, Saudi Arabia

<sup>b</sup> Institute of Energy Technologies and Centre for Research in Nanoengineering, Universitat Politècnica de Catalunya, Diagonal 647, 08028 Barcelona, Spain

<sup>c</sup> Department of Chemistry, University of Aberdeen, Aberdeen, UK

## ARTICLE INFO

### Article history:

Received 18 December 2015

Received in revised form 27 March 2016

Accepted 29 March 2016

Available online 29 March 2016

### Keywords:

Cerium oxide

Ruthenium/cerium oxide

Ethanol reforming reaction

Ethanol TPD

Water gas shift

Temperature programmed desorption

## ABSTRACT

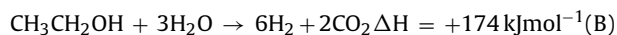
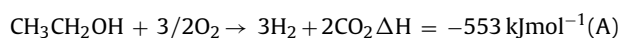
The reaction of ethanol has been investigated on Ru/CeO<sub>2</sub> in steady state conditions as well as with temperature programmed desorption (TPD). High resolution transmission electron microscopy (HRTEM) images indicated that the used catalyst contained Ru particles with a mean size of ca. 1.5 nm well dispersed on CeO<sub>2</sub> (of about 12–15 nm in size). Surface uptake of ethanol was measured by changing exposure to ethanol followed by TPD. Saturation coverage is found to be between 0.25 and 0.33 of a monolayer for CeO<sub>2</sub> that has been prior heated with O<sub>2</sub> at 773 K. The main reactions of ethanol on CeO<sub>2</sub> during TPD are: re-combinative desorption of ethanol; dehydrogenation to acetaldehyde; and dehydration to ethylene. The dehydration to ethylene occurs mainly in a small temperature window at about 700 K and it is attributed to ethoxides adsorbed on surface-oxygen defects. The presence of Ru considerably modified the reaction of ceria towards ethanol. It has switched the desorption products to CO, CO<sub>2</sub>, CH<sub>4</sub> and H<sub>2</sub>. These latter products are typical reforming products. Ethanol steam reforming (ESR) conducted on Ru/CeO<sub>2</sub> indicated that optimal reaction activity is at about 673 K above which CO<sub>2</sub> production declines (together with that of H<sub>2</sub>) due to reverse water gas shift. This trend was well captured during ethanol TPD where CO<sub>2</sub> desorbed about 50 K below than CO on both oxidized and reduced Ru/CeO<sub>2</sub> catalysts.

© 2016 Elsevier B.V. All rights reserved.

## 1. Introduction

Hydrogen generation from renewables and its use as a clean fuel is attractive since upon oxidation only water is formed while the released energy is the highest known per unit weight of a chemical compound (120.7 kJ/g). Because low molecular weight oxygenates can be stored and distributed readily they are used as hydrogen carriers for on-board generation. Methanol and ethanol, in particular, are promising liquid feeds for onboard hydrogen production due to their high hydrogen to carbon (H/C) atomic ratio. Steam reforming of oxygenated hydrocarbons for the production of hydrogen is thermodynamically more favored at relatively low temperatures compared with that of hydrocarbons [1]. A major advantage of ethanol production from biomass and its use for the energy generation is the absence of carbon emissions because carbohydrates are initially formed by photosynthesis. Producing hydrogen from the catalytic decomposition of ethanol has been investigated for almost

two decades now. The two main reactions are partial oxidation (Reaction A), and steam reforming (Reaction B).



Reaction B, despite being energetically more demanding than Reaction A, yields more hydrogen and can be achieved with high selectivity. The reaction requires a catalyst with three main properties. First, it should be capable of breaking the C–C bond of the adsorbed ethoxide (formed upon dissociative adsorption on the catalysts surface). Second, it needs to be active for water gas shift (WGS) and reforming reactions. Third, it needs to have fast hydrogen–hydrogen bond generation kinetics [2]. Therefore, a combination of a reducible metal oxide and metals capable of both C–C bond dissociation and water gas shift reaction is needed.

CeO<sub>2</sub> is one of the most active redox binary metal oxides [3] known. Part of the reasons is the low activation energy for O anions diffusion [4] and the relatively low oxygen vacancy formation energy [5]. In addition to its use in automobile catalytic converters [6], and as a WGS support [7] it was also, for the same reasons, found to be an excellent support for reforming of ethanol. Our groups have previously studied the reactions of ethanol oxidation

\* Corresponding author.

E-mail address: [idirish@sabic.com](mailto:idirish@sabic.com) (H. Idriss).

and steam reforming by infrared (IR) spectroscopy, and temperature programmed desorption (TPD), over  $\text{CeO}_2$  [8],  $\text{Pd/CeO}_2$  [8],  $\text{Pt/CeO}_2$  [9],  $\text{Rh/CeO}_2$  [10],  $\text{Pt-Rh/CeO}_2$  [11],  $\text{Pd-Rh/CeO}_2$  [12],  $\text{Au/CeO}_2$  [13],  $\text{Au-Rh/CeO}_2$  [14] and  $\text{Rh/CeO}_2\text{-ZrO}_2$  [15]. The most active of these catalysts was the  $\text{Rh-Pd/CeO}_2$  [16]. Many other researchers have also worked on this reaction and a large number of catalysts based on other metals and oxides have been synthesized and tested [17–20]. While the use of non-noble metals is possible, noble metals, in particular Pt and Pd are unique, as they do not form coke and therefore are not easily poisoned to deactivation. In brief, a metal such as Rh is needed for efficient C–C bond dissociation. It is to be noted that Rh has a unique role within the 4d transition metals for C–H bond dissociation reaction [21], a requirement prior to the C–C bond dissociation reaction, and Pt (or Pd) is needed for fast hydrogen–hydrogen recombination reactions, while  $\text{CeO}_2$  provides the active support for the redox process. Ru is akin to Rh in many properties (such as for C–C and C–H bond breaking reactions). Its introduction onto  $\text{CeO}_2$  and  $(\text{CeZr})\text{O}_2$  has shown benefits for hydrogen production from glycerol [22]. Ru based catalysts have been studied previously for steam reforming of ethanol [23], oxidative steam reforming [24],  $\text{CO}_2$  activation [25], and ammonia synthesis [26]. Previously we have synthesized and conducted preliminary studies on  $\text{Ru-Pt/CeO}_2$  on the water gas shift reaction [27] and found it to be of high activity.

In this work, we limit our attention on  $\text{CeO}_2$  and  $\text{Ru/CeO}_2$  in order to determine the reaction mechanisms of ethanol where investigation of elementary steps can be extracted. Among the many reactions that ethanol can have on the surface of  $\text{CeO}_2$  are dehydrogenation to acetaldehyde [28], dehydration to ethylene, oxidation to acetates, condensation to higher aldehydes, and other C–C bond making reactions [29,30]. The addition of Ru (initially in the form of  $\text{RuO}_2$ ) is poised to change these reactions and accelerate the C–C bond dissociation reaction resulting in WGS and reforming reactions. We also attempt to link TPD results to catalytic performances in order to probe into the reforming reaction.

## 2. Experimental

### 2.1. Catalyst preparation

Cerium oxide ( $\text{CeO}_2$ ) was prepared via precipitation from a solution of white crystalline cerous nitrate,  $(\text{Ce}(\text{NO}_3)_3 \cdot 6\text{H}_2\text{O})$  (100 g), in deionised water (0.40 L) with mild stirring. The temperature was kept constant at 373 K (pH 8–8.5) and ammonia ( $0.91 \text{ mol L}^{-1}$ ) was added drop wise (ca. 30 mL). The resulting white precipitate was collected by filtration, washed with deionised water and left to dry in an oven for 12 h (373 K) before being calcined (773 K) for 4 h under air-flow. Ruthenium (III) chloride (0.5008 g) was dissolved in approximately 150 mL of double distilled water and stirred using a magnetic stirrer. Once the salt had dissolved in the water, a dark solution was formed (without the formation of a precipitate). The solution was then transferred to a standard volumetric flask (1 L) and made up to the 1000 mL with double distilled water. The resulting solution was stirred to ensure a homogenous mixture was produced.  $\text{Ru/CeO}_2$  was prepared using the impregnation method. 0.5 wt.% of Ru metal was calculated relative to 5 g of the total amount of catalyst and the correct amount of metal stock solution was obtained. The accurate amount of cerium oxide was added into a beaker before adding the metal chloride solutions. The resulting solution was then stirred and heated slowly in a beaker wrapped in aluminium foil in order to maintain homogenous heating. Care was taken to ensure the temperature remained constant at 373 K until the majority of liquid had vaporised. The resulting dark paste-like material was then dried overnight in the oven at 373 K. Upon drying, the catalyst underwent calcinations in the open-ended fur-

nace at 673 K for 3 h under air-flow. The final product was grounded into a fine powder and is used as the catalyst.

### 2.2. Catalyst characterisation and reaction conditions

The surface area of  $\text{CeO}_2$  and  $\text{Ru/CeO}_2$  determined using the Brunauer, Emmett and Teller (BET) was found to be  $\sim 55 \text{ m}^2/\text{g}$  and changed very little with metal deposition (0.5 wt.%).

High-Resolution Transmission Electron Microscopy (HRTEM) was carried out at 200 kV with a JEOL JEM 2100 instrument equipped with a  $\text{LaB}_6$  source. The point-to-point resolution of the microscope was 0.19 nm. Samples were deposited on holey-carbon-coated Cu grids from alcohol suspensions. For each sample, more than one hundred particles were used for particle size distribution calculation. Local structural information from individual metal particles was obtained by Fourier filtering.

Temperature-programmed reduction (TPR) analyses were performed in a sample quartz tube coupled to a thermal conductivity detector (AutoChem 2920, Micrometrics). A mixture of 10%  $\text{H}_2$  in Ar was flowed through the sample, and the temperature was raised at a heating rate of  $10^\circ\text{C min}^{-1}$  and consumption of the  $\text{H}_2$  was monitored by Thermal Conductivity Detector (TCD).  $\text{H}_2$  consumption was pre-calibrated so that extraction of moles required per unit weight of the materials reduction was made possible.

Ethanol Temperature programmed desorption (TPD) of  $\text{CeO}_2$  and  $\text{Ru/CeO}_2$  was performed in U-shaped quartz fixed bed micro reactor at atmospheric pressure. Samples (100 mg) were loaded onto the sinter of the reactor where, prior to any reactions, the sample catalysts were either reduced or oxidized at  $450^\circ\text{C}$  overnight under hydrogen or oxygen flow, respectively. The reaction chamber was then allowed to cool to room temperature with continuous gas flow. The reactor was then pumped down to base pressure ( $\sim 10^{-2}$  Torr) by a roughing pump to remove any loosely adsorbed gas on the surface of the catalyst and to clean the reaction line. This would typically take 15–20 min. The system was then pumped further by the diffusion pump to pressures of ca.  $10^{-7}$  Torr. Typically this took around 30–60 min. Ethanol was injected using a micro-syringe onto the surface of the catalyst and was left for around 15 mins. The system was then pumped for a further hour using both the roughing and diffusion pumps to remove any loosely adsorbed ethanol molecules on the catalyst surface and in the reaction line. A constant pressure of  $\sim 10^{-5}$  Torr was again achieved in the high vacuum chamber (HVC). Following this, the reactor was placed into a high temperature-heating furnace, which was connected to a programmed temperature controller. A thermocouple was placed into the furnace in which the tip was in-line with the reactor bed. To measure the desorption profiles a quadrupole mass spectrometer was used. The quadrupole mass spectrometer was connected to a computer running mass spectrometer software (RGA for Windows). The quadrupole mass spectrometer was then started and the signal at  $m/z=31$  (principal fragment of ethanol) was monitored before any data was collected. Once the signal at  $m/z=31$  stabilized, the other fragments were monitored in the same way. The experiment began when all 12 fragments (maximum number to be recorded per run) had stabilized at which the temperature controller was also started simultaneously. The reaction was initiated at room temperature and the furnace was heated at a linear rate of  $20 \text{ K/min}^{-1}$ . The scan rate for the 12 masses was approximately 5 s per scan. Quantitatively, the peak area under each peak was calculated using the trapezoidal method which is an approximation for computing the total area under a series of data points. The correction factor for each individual fragment was then calculated. Normalization of each desorption profile was obtained by multiplying the product desorption spectrum by the correction factor. Contributions of different masses were subtracted. For example in the case of ethanol the  $m/e$  29 signal resulting from ethanol

fragmentation was subtracted from the total signal observed. The remaining is largely due to acetaldehyde. More details on the method can be found in many of our previous work [31]. The relative yields were calculated for individual desorption products by quantitatively analysing the desorption spectra for the respective mass fragments. Due to the possibility of more than one products desorbing at similar temperature and similar mass fragment signals, care is needed when analysing the result of the desorption profile. The fragmentation patterns of all identified products were recorded using the same set up to assign the contribution of a fragment to another fragment in case of two or more products desorbing at the similar temperature. The desorbed products were determined by assigning all mass fragment as a function of temperature, intensity and correlation with other mass fragment peaks. Any peak that could be assigned to a single product was first identified and contribution of its mass fragments to the mass fragments of other desorbed products were subtracted. This process was continued until all desorption profiles were accounted for. This approach is described in more details in numerous previous work [8,9,32].

The percent yield of each species as a fraction of the total amount of desorbed products and carbon selectivity as a fraction of the total carbon desorbed were calculated using the following equations:

$$Y_i = [(PA_i \times CF_i) / \sum (PA_j \times CF_j)] \times 100$$

$$Y_{Ci} = [(PA_i \times CF_i \times N_{Ci}) / \sum (PA_j \times CF_j \times N_{Cj})] \times 100$$

where  $Y_i$  is the product yield,  $PA$  is the area underneath the peak,  $CF_i$  is the correction factor (relative to CO),  $Y_{Ci}$  is the percent carbon yield,  $N_{Ci}$  is the number of carbon atoms present in the product  $i$ .

The mass fragment desorption spectra are corrected to reflect reaction rate, and to allow relative product yields to be obtained. The correction factor,  $CF$ , relative to CO for product is given as:

$$CF_i = \frac{1}{I_x \times F_m} \sum_j \frac{F_m}{G_m \times T_m}$$

where  $I_x$  is the ionization efficiency,  $F_m$  is the mass fragment yield,  $G_m$  is the electron multiplier gain, and  $T_m$  is quadrupole transmission.

The ionization efficiency is dependent on the number of electrons per molecule ( $n_e$ ). A correction for the total ionization efficiency of a molecule relative to CO is given by:

$$I_x = 0.6 \left( \frac{n_e}{14} \right) + 0.4$$

The gain of the electron multiplier, a function of ion mass, relative to CO, is approximated as

$$G_m = \left( \frac{28}{MW} \right)^{\frac{1}{2}}$$

Transmission of an ion through the quadrupole filter, a function of ion mass, is approximated by

$$T_m = 10 \frac{(30 - MW)}{155} \quad MW > 30$$

$$T_m = 1 \quad MW < 30$$

Thus, one has to calculate the  $CF$  for each fragment for each product in order to perform quantitative analysis of the TPD data. The normalization of desorption profiles were obtained by multiplying the product desorption spectrum by the correction factor.

Catalytic reactions were performed in a flow system where out-gassed pre-mixed ethanol/water were put in an “injector”: a

**Table 1**

Analysis of the desorption products following ethanol-TPD on oxidized ceria ( $CeO_2$ ) at 300 K. Associated TPD data is shown in Fig. 1.

Product	Peak Desorption Temperature (K)	% Carbon Yield	% Carbon Selectivity
Ethylene	640	2.81	22.5
Carbon Monoxide	640	0.47	3.75
Acetaldehyde	475	8.61	69.00
Ethanol	475	87.31	–
Furan	640	0.56	4.70

stainless steel pump programmed to inject the liquid (reactant) into the reactor at different preset volumetric rates. The powdered catalyst (0.5 g) was placed inside a tubular reactor on a fritted glass of medium pores that is kept in a cylindrical furnace. The reactor 44 cm long and 2 cm in diameter is a cylindrical tube made of a 316 stainless steel material. After the injector and the reactor were connected the flow rate of reactant over the catalyst is determined. Rate of gas production was measured using a volumetric flow meter. Gas was sampled (0.2 mL) at different temperatures and times and injected into the two GCs for analysis of  $H_2$ ,  $CH_4$ , CO and  $CO_2$ . All the experiments were performed at a steady state condition, where the catalytic reaction rate was constant. Approximately 10 measurements were taken for the sample gas at each temperature and inlet flow rate.

### 3. Results and discussions

#### 3.1. TPD results of oxidised and reduced $CeO_2$

Fig. 1 presents TPD results following surface saturation with ethanol of oxidized ceria ( $CeO_2$ ) at 300 K. Two main desorption regions are present, one at low temperature  $\sim 475$  K and the other at high temperature  $\sim 640$ – $650$  K. In addition, minor desorption features appear at  $\sim 560$  K as shown in Fig. 1B. Fig. 1A shows the main desorption products; ethanol ( $CH_3CH_2OH$ ,  $m/z = 31, 29, 27, 43$ ), acetaldehyde ( $CH_3CHO$ ,  $m/z = 29, 43$ ), and ethylene ( $m/z = 27, 28$ ). The major desorption species is unreacted ethanol accounting for  $\sim 87\%$  of the total carbon desorbed during heating to 750 K. Both ethanol and acetaldehyde desorb, simultaneously, in the low temperature desorption region at  $\sim 475$  K. The simultaneous desorption of ethanol and acetaldehyde at around 390 K has also been observed previously in TPD spectra obtained following the adsorption of acetaldehyde on  $CeO_2$  [28] and at ca. 450 K following adsorption of ethanol [8]; both at 300 K. Ethanol desorption is made upon hydrogenation of acetaldehyde in acetaldehyde-TPD and acetaldehyde desorption is made by ethanol dehydrogenation in ethanol-TPD. This simple example of micro-reversibility also shows the potential of  $CeO_2$  for oxidation (to acetaldehyde) and reduction (to ethanol) reactions. The desorption at lower temperature in the case of acetaldehyde is linked to its weaker adsorption energy when compared to that of ethanol. Aldehydes in general adsorb on metal oxides via an oxygen lone pair interaction with metal cations [33,34] ( $Ce^{4+}$  in this case) while alcohols adsorption occurs via dissociative adsorption on a pair of metal cation-oxygen anion [35] ( $Ce^{4+}-O^{2-}$  in this case). The symmetrical desorption of ethanol TPD peak as a function of coverage (data not shown) suggests a second order desorption due to re-combinative ethanol desorption from ethoxide and a proton of the surface hydroxyls of  $CeO_2$  sites. Acetaldehyde desorption contributed by a carbon yield of approximately 9% at  $\sim 475$  K. In the high temperature region around 640 K, a small amount (Table 1) of CO and ethylene desorb; peaks of  $m/z = 28$ , and  $m/z = 27, 28$ , respectively, due to dehydration of a small fraction of ethoxides left on the surface. The adsorption energy of ethanol has been recently computed by density functional theory (DFT) calculation and it is found to be stronger on

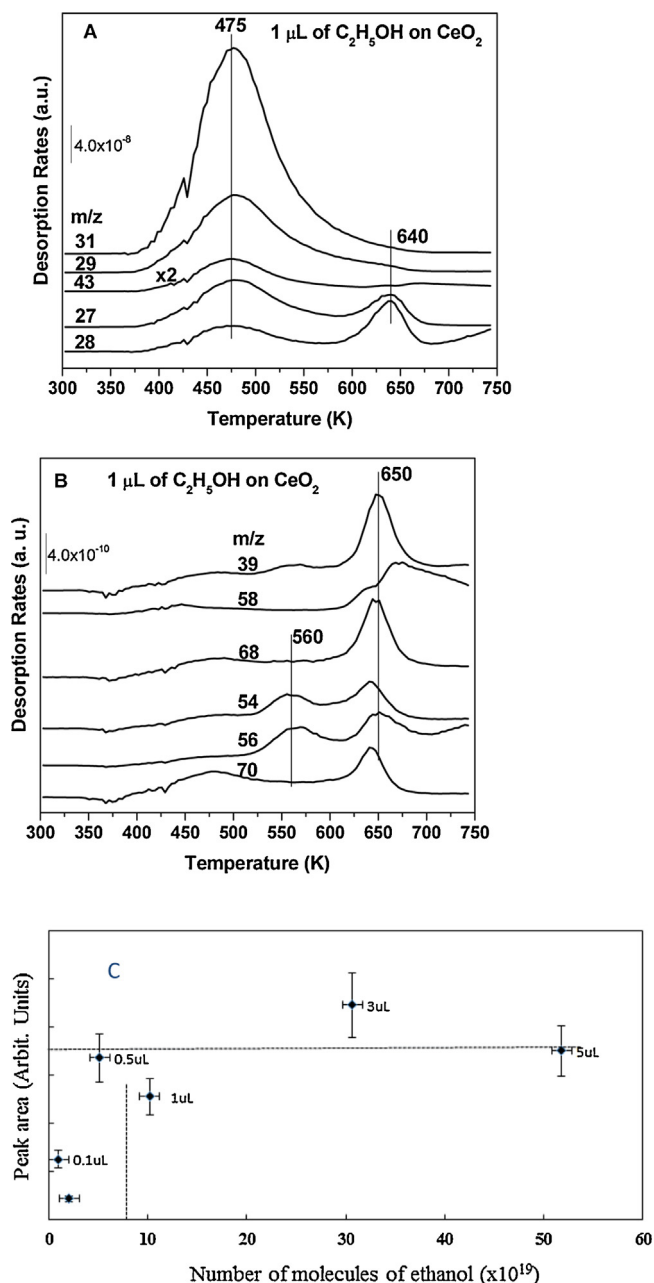


**Fig. 1.** TPD spectra obtained after the injection of 1 μL (surface saturation) of ethanol on CeO<sub>2</sub> at 300 K. (A) main desorption products; ethanol ( $m/z=29, 31$ ), acetaldehyde ( $m/z=43, 29$ ), and ethylene ( $m/z=27, 28$ ). (B) minor products; acetone ( $m/z=58$ ), furan ( $m/z=39, 68$ ), butadiene ( $m/z=39, 54$ ), butene ( $m/z=56$ ), and crotonaldehyde ( $m/z=70$ ). (C) A plot of peak area of ethanol ( $m/z=31$ ) peak as a function of number of molecules of ethanol injected on CeO<sub>2</sub>.

surface oxygen defects when compared to that on stoichiometric sites [36]. By analogy, this small channel can be linked to surface oxygen defects on which ethoxides are more stabilized.

Fig. 1B shows minor desorption products; acetone ( $m/z=58$ ), furan ( $m/z=39, 68$ ), butadiene ( $m/z=39, 54$ ), butene ( $m/z=56$ ), and crotonaldehyde ( $m/z=70$ ). Butene and butadiene desorb at 560 and 650 K temperatures. Acetone, crotonaldehyde, and furan desorb at ~650 K. CO and furan ( $m/z=39, 68$ ) desorb with the carbon yields of ~0.5, and 0.6% (Table 1), respectively. The desorption of water ( $m/z=18$ ), which was observed all the systems studied here, occurs at 475 K (data not shown). A very small amount of hydrogen ( $m/z=2$ ) also desorb at 635 K (data not shown). The origin of these products has been studied in details in many of previous work and

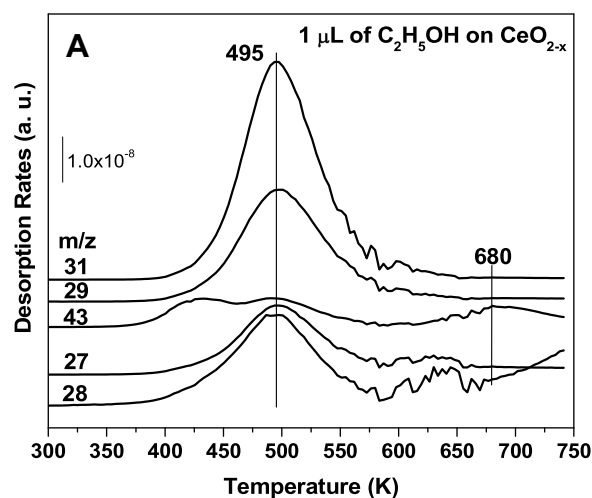
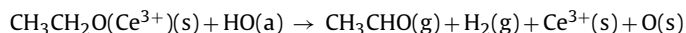


**Fig. 2.** A. TPD spectra obtained for main products; ethanol ( $m/z=29, 31$ ), acetaldehyde ( $m/z=43$ ), and ethylene ( $m/z=27, 28$ ), after the injection of 1 μL of ethanol on H<sub>2</sub>-reduced CeO<sub>2</sub>.

details on which can be found in references [37,38]. These will not be further explained for the sake of focusing on the main reaction products.

Fig. 1C is the plot of peak area of ethanol ( $m/z=31$ ) TPD peak as a function of number of molecules of ethanol injected on CeO<sub>2</sub>. This figure shows that the saturation coverage of ethanol is achieved by an amount > 0.5 μL ethanol (ca. 10<sup>-5</sup> moles or 5 × 10<sup>18</sup> molecules) for 100 mg of CeO<sub>2</sub> (or about 5 × 10<sup>19</sup> molecules/g<sub>CeO<sub>2</sub></sub>). Given that the BET surface area of CeO<sub>2</sub> is 55 m<sup>2</sup> then there is about 1 – 2 × 10<sup>18</sup> molecules of ethanol/m<sup>2</sup><sub>CeO<sub>2</sub></sub>. This value would certainly change depending on the extent of hydroxylation of the surface prior to adsorption but still gives an indication of surface saturation between 1/4 and 1/3 of a monolayer with respect to Ce cations (the area of unit cell of CeO<sub>2</sub> (111), the most stable surface, is equal to 13.1 × 10<sup>-20</sup> m<sup>2</sup> (taking Ce–Ce distance of 3.89 × 10<sup>-10</sup> m); in other words there are about 2.5 × 10<sup>18</sup> atoms of Ce cation in 1 m<sup>2</sup>). In these experiments CeO<sub>2</sub> was heated to 450 °C in O<sub>2</sub> and cooled down under oxygen.

Fig. 2 presents similar TPD but after CeO<sub>2</sub> was H<sub>2</sub>-reduced at 450 °C overnight and cooled down under hydrogen; denoted CeO<sub>2-x</sub>. Two main observations can be extracted from this TPD when compared to that of CeO<sub>2</sub>. First not much desorption is seen at the high temperature channel. Second, while most desorption occurs at about 500 K the desorption profile is different. A large fraction of the desorbed molecules is composed of the reaction products: acetaldehyde and ethylene. The shift to lower temperature might be due to a more reactive surface where the presence of surface oxygen defects have accelerated ethanol reaction more than stabilizing it. The desorption of ethylene (dehydration) can be rationalized as due to the increase of these surface oxygen defects sites created by reduction and therefore the driving force would be to heal them. The increased production of acetaldehyde is not as simple to explain. We have previously studied ethanol adsorption on O defected CeO<sub>2</sub> surfaces [36]. Based on the adsorption modes found we may view the process of ethanol (or ethoxides) dehydrogenation to acetaldehyde on a reduced surface as follow



In other words, the process does not involve a change in the oxidation of Ce<sup>3+</sup> so it inevitably competes with the dehydration reaction, the latter results in Ce<sup>3+</sup> oxidation to Ce<sup>4+</sup>. The desorption of acetaldehyde at lower temperature than that observed on oxidized CeO<sub>2</sub> is viewed as due to a lowering of the activation energy



for the reaction since acetaldehyde desorption at this temperature is reaction limited (and not desorption limited) [see desorption of acetaldehyde in acetaldehyde TPD in [28]]. The amount of unreacted ethanol drops to about 10% of the total desorption products.

In order to study the effect of Ru on the reaction of  $\text{CeO}_2$  we have performed Ethanol-TPD on both the oxidized and reduced surfaces. Prior to analysing and discussing ethanol-TPD it is worth presenting TPR and TEM of the Ru/ $\text{CeO}_2$  catalyst.

### 3.2. TPR

The TPR profiles of  $\text{CeO}_2$ , 1 wt% Ru- $\text{CeO}_2$ , and 1 wt% Pt- $\text{CeO}_2$  are shown in Fig. 3.  $\text{CeO}_2$  is presented for comparison and Pt/ $\text{CeO}_2$  is used as it has been studied by others numerous times. We have initially presented TPR of  $\text{CeO}_2$  which represents two temperature domains. The low temperature domain representing a complex structure of two peaks (between about 300 and 450 °C) is attributed to surface reduction while the high temperature one about 600 °C is attributed to bulk reduction. This interpretation is based on results of successive TPR where the BET surface area constantly decreases due to the high temperature reached at the end of the TPR run (ca. 1000 °C) and where gradually the first temperature domain decreases until becoming of negligible contribution. In the case of M/ $\text{CeO}_2$  one can get the same structures related to  $\text{CeO}_2$  shifting to

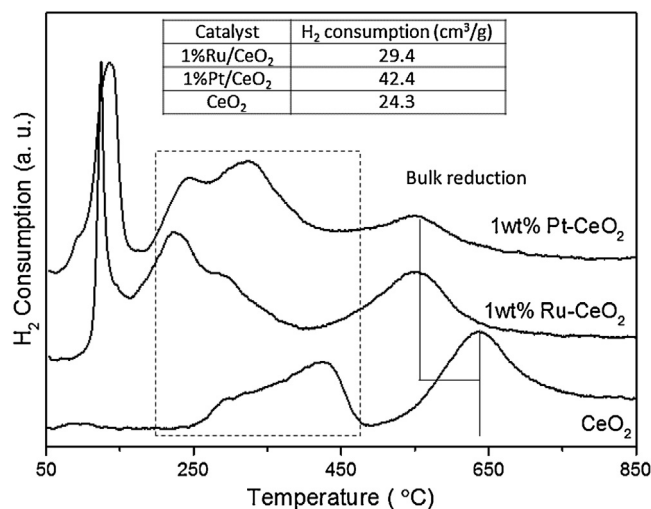


Fig. 3. TPR profiles of  $\text{CeO}_2$ , 1 wt.%Ru/ $\text{CeO}_2$ , and 1 wt.%Pt/ $\text{CeO}_2$ .

lower temperature. This is attributed to spill over of hydrogen from the metal surface to the oxide surface accelerating its reduction by about 100 K each. While the lowering of surface reduction tem-

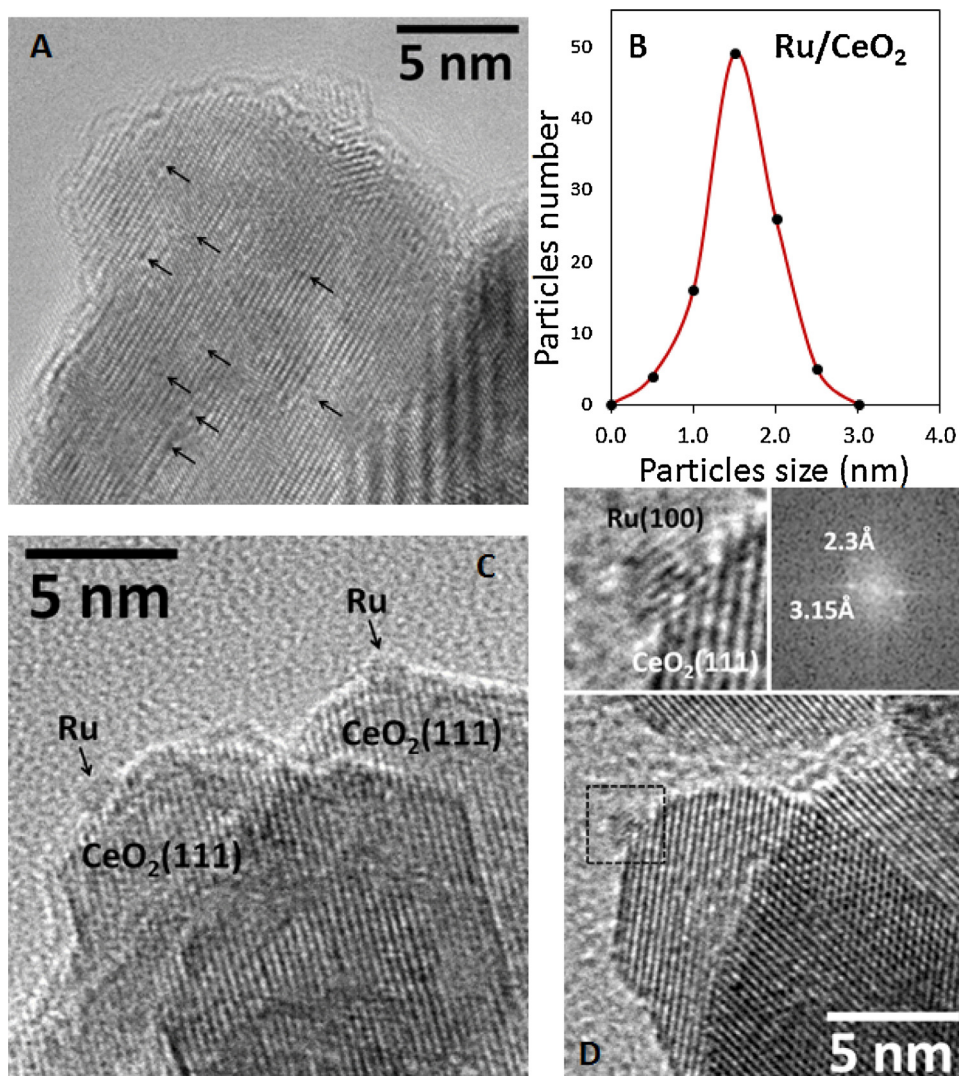


Fig. 4. HRTEM images of 0.5 wt.% Ru/ $\text{CeO}_x$  (A) before and (C-D) after the reaction with ethanol. (B) Ru particle size distribution.

**Table 2**

Reaction products and conversion at different temperatures and with different inlet flow rates during ethanol steam reforming (3/1 molar ratio of EtOH/H<sub>2</sub>O) on 0.5 wt.% Ru/CeO<sub>2</sub>.

	mol/mL	mol/mL	mol/mL	mol/mL	mL/min <sup>-1</sup> g <sub>Catal.</sub> <sup>-1</sup>	%
T(K)	H <sub>2</sub>	CO	CH <sub>4</sub>	CO <sub>2</sub>	Flow rate	Conversion
573	3.3 × 10 <sup>-5</sup>	5.2 × 10 <sup>-6</sup>	7.3 × 10 <sup>-6</sup>	4.5 × 10 <sup>-6</sup>	20.5	13.5
673	4.5 × 10 <sup>-5</sup>	4.8 × 10 <sup>-6</sup>	4.4 × 10 <sup>-6</sup>	8.9 × 10 <sup>-6</sup>	54	36
773	1.9 × 10 <sup>-5</sup>	6.9 × 10 <sup>-6</sup>	1.5 × 10 <sup>-6</sup>	8.5 × 10 <sup>-6</sup>	84	56
<sup>a</sup> Inlet flow mL <sub>liquid</sub> h <sup>-1</sup> g <sub>Catal.</sub> <sup>-1</sup> (mL <sub>gas</sub> /min <sup>-1</sup> g <sub>Catal.</sub> <sup>-1</sup> )						
5 (150)	1.7 × 10 <sup>-5</sup>	7.0 × 10 <sup>-6</sup>	1.6 × 10 <sup>-6</sup>	6.8 × 10 <sup>-6</sup>	126	84
7.5 (224)	1.6 × 10 <sup>-5</sup>	7.9 × 10 <sup>-6</sup>	1.0 × 10 <sup>-6</sup>	5.4 × 10 <sup>-6</sup>	138	61
10 (300)	1.8 × 10 <sup>-5</sup>	8.5 × 10 <sup>-6</sup>	1.2 × 10 <sup>-6</sup>	6.4 × 10 <sup>-6</sup>	131	44

<sup>a</sup> Reactions as a function of flow rate is performed at 823 K.

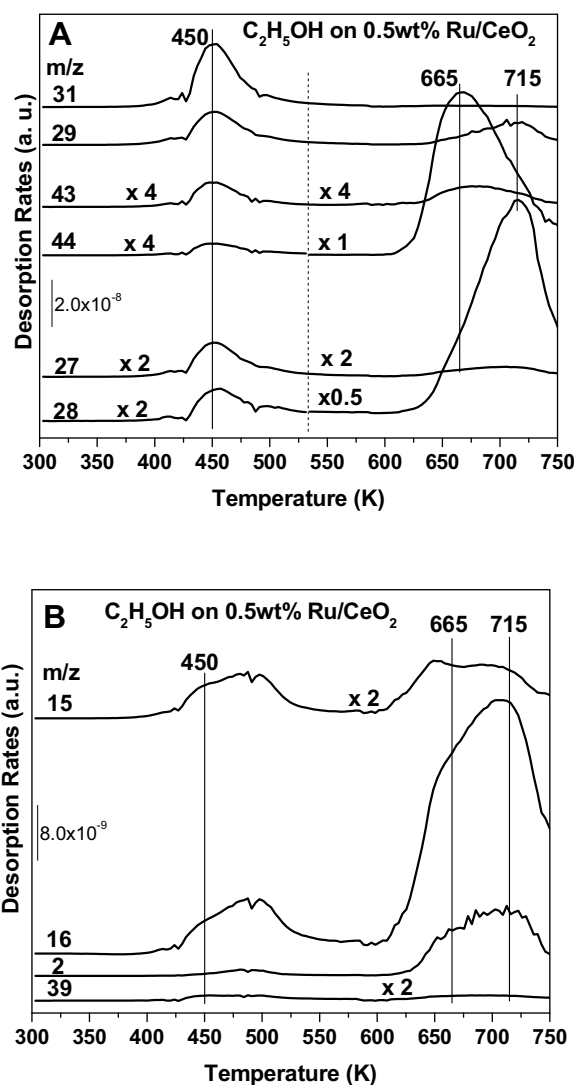
perature can be easily understood that of bulk reduction involves oxygen diffusion from the bulk to the surface accelerated by the constant creation of surface oxygen defects due to the presence of the metal. The effect of metal on the reduction of support has been investigated for many systems. Within this context the reduction of surface CeO<sub>2</sub> has been shown to be accelerated by the presence of Pt computationally using the DFT+U method [39,40], by the presence Rh experimentally using XPS and TPD [41], and by the presence of Pd and Rh computationally also using the DFT+U method [36]. In particular, it has been reported that the decrease in the energy required to transfer oxygen atoms from CeO<sub>2</sub>(111) to Pt<sub>8</sub> decreases from 2.25 eV to about 1 eV [39]. In addition, a clear peak is seen between 120 and 150 °C in both cases (for Ru and for Pt). It is to be noted that Ru peak reduction is very sharp when compared to that of Pt. As will be seen in the HRTEM results this may be linked to the very narrow particle size distribution of Ru particles. Quantitative analyses indicated that the total amount of H<sub>2</sub> consumed is higher on Pt/CeO<sub>2</sub>, when compared to Ru/CeO<sub>2</sub>, and can be explained as due to the more pronounced spillover of hydrogen from Pt to CeO<sub>2</sub>.

### 3.3. HRTEM images of 0.5 wt.% Ru/CeO<sub>2</sub>

Ethanol-TPD and ethanol steam reforming catalytic reactions (see below) were conducted on 0.5 wt.% Ru/CeO<sub>2</sub>. HRTEM images of this 0.5 wt.% Ru/CeO<sub>2</sub> before and after the reaction are shown in Fig. 4. While CeO<sub>2</sub> particles are the main observed ones the presence of some Ru particles, indicated by arrows in the representative HRTEM view of the fresh sample of Fig. 4A, is possible. The used (reduced) sample however contains CeO<sub>2</sub> on which well-dispersed Ru crystallites with a mean particle size of only 1.5 nm (Fig. 4B) are visible. It merits to be highlighted that the particle size distribution of Ru is very narrow and more than 90% of them lie in the range of 1–2 nm. There is no evidence of carbon deposition in any part of the sample. Fig. 4C shows a representative HRTEM figure of this catalyst. (111) CeO<sub>2</sub> lattice fringes of support particles are recognized along with small Ru particles. Fig. 4D shows another representative HRTEM image of the sample along with a detailed enlargement of the area enclosed in the square with its corresponding FT image. The intense spots at 3.15 Å correspond to the (111) planes of the CeO<sub>2</sub> crystallite support, and the weak spots at 2.3 Å are ascribed to (100) planes of the Ru metal particles, visible in profile view.

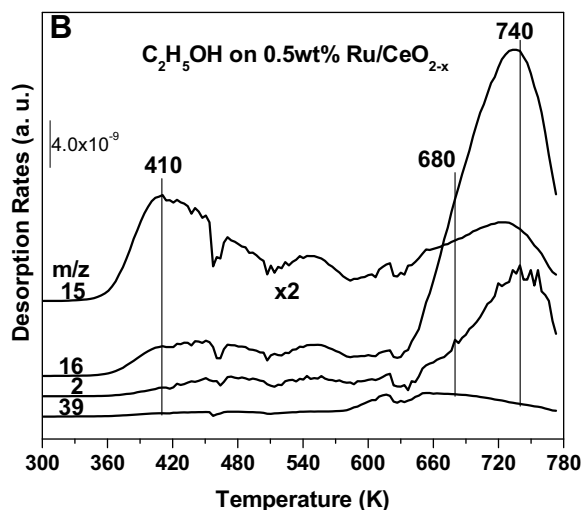
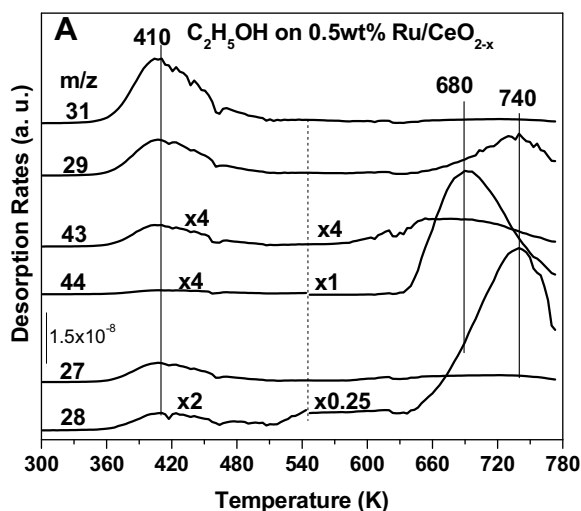
### 3.4. TPD results of 0.5 wt.% Ru/CeO<sub>2</sub>

Fig. 5 shows TPD results obtained following saturated adsorption of ethanol on 0.5 wt.% Ru/CeO<sub>2</sub> at 300 K. Unreacted ethanol (CH<sub>3</sub>CH<sub>2</sub>OH, *m/z*=31, 29, 27, 43) as well as products derived from ethanol such as acetaldehyde (CH<sub>3</sub>CHO, *m/z*=m/z=29, 43, 44), CO (*m/z*=28), CO<sub>2</sub> (*m/z*=44), CH<sub>4</sub> (*m/z*=16, 15), ethylene (C<sub>2</sub>H<sub>4</sub>, *m/z*=27, 28), and H<sub>2</sub> (*m/z*=2) are seen to desorb. At 450 K, ethanol, acetaldehyde, and ethylene desorb from the surface as shown in Fig. 5A. The comparison with the TPD results of CeO<sub>2</sub> with and



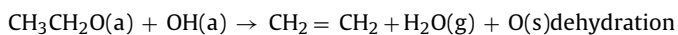
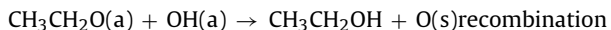
**Fig. 5.** TPD spectra obtained after the injection of 5  $\mu$ L of ethanol on 0.5 wt.% Ru/CeO<sub>2</sub>. (A) main products; ethanol (*m/z*=29, 31), acetaldehyde (*m/z*=43), ethylene (*m/z*=27, 28), carbon monoxide (*m/z*=28), and carbon dioxide (*m/z*=44). (B) Minor products; methane (*m/z*=15, 16), hydrogen (*m/z*=2), and furan (*m/z*=39).

without Ru clearly shows the effect of the metal on the reactivity towards ethanol decomposition. The amount of the unreacted ethanol (CH<sub>3</sub>CH<sub>2</sub>OH, *m/z*=31, 29, 27, 43) desorbing from 0.5 wt.% Ru/CeO<sub>2</sub> is significantly reduced when compared with oxidized CeO<sub>2</sub> without Ru. This increase in reactivity is reflected in the increased yields of the other products. Ethanol desorb alongside ethylene and acetaldehyde at ~450 K, which is 25 K lower than the desorption temperature on oxidized CeO<sub>2</sub>. The competition



**Fig. 6.** TPD spectra obtained after the injection of 5  $\mu\text{L}$  of ethanol on 0.5 wt.% Ru/CeO<sub>2-x</sub>. (A) main products; ethanol ( $m/z = 29, 31$ ), acetaldehyde ( $m/z = 43$ ), ethylene ( $m/z = 27, 28$ ), carbon monoxide ( $m/z = 28$ ), and carbon dioxide ( $m/z = 44$ ). (B) Minor products; methane ( $m/z = 15, 16$ ), hydrogen ( $m/z = 2$ ), and furan ( $m/z = 39$ ).

between re-combinative desorption, dehydrogenation and dehydration can thus be observed at this reaction channel.



These three reactions are however minor on the surface of Ru/CeO<sub>2</sub> as at high temperature most of the reaction products are CO, CO<sub>2</sub>, H<sub>2</sub> and CH<sub>4</sub>. The high temperature channel merits some attention as it appears to be mainly originating from a combination of reforming and water gas shift reaction products. Qualitatively, because most of desorption occurs at high temperature, surface diffusion of adsorbate takes place and are trapped at high energy sites at the interface between Ru and CeO<sub>2</sub>. At high temperatures, these species, requiring both Ru and CeO<sub>2</sub> for the reactions, are in the temperature domain of WGS and methane reforming. It is to

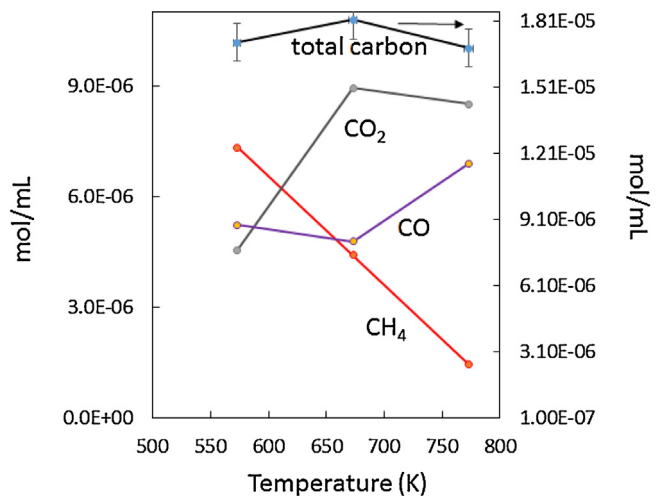


**Fig. 7.** CO, CO<sub>2</sub> and CH<sub>4</sub> product distribution during steam ethanol reforming over Ru/CeO<sub>2</sub> as a function of temperature. More data can be found in Table 2.

be noted that CO<sub>2</sub> desorb at about 50 K lower than CO. Together with CO<sub>2</sub> desorption CH<sub>4</sub> and H<sub>2</sub> occurs. In other words, adsorbed ethoxides on these high stable surface sites at the vicinity of Ru, given enough energy, are decomposed to CH<sub>4</sub> and CO, which in turn react with surface hydroxyls to give CO<sub>2</sub> and H<sub>2</sub>. It is not possible to accurately quantify the hydrogen amounts as the sensitivity of the quadrupole mass spectrometer is too low for  $m/z = 2$ ; so the desorption trace of  $m/z = 2$  can be taken only as a guide. It is interesting to note the presence of two desorption domains for CH<sub>4</sub>. One at the CO<sub>2</sub> desorption and the other at the CO desorption; this can be seen following  $m/z = 15$ . If the switch between CO<sub>2</sub> and CO is strictly thermodynamic, WGS is exothermic, then would have not expected two desorption domains for CH<sub>4</sub>. It is possible to attribute these two desorptions to an in situ reduction of Ru oxide by hydrogen produced at the initial phase of the reaction (at about 600 K). To further probe into this reaction dynamics Ethanol-TPD, following saturation of the prior hydrogen reduced 0.5 wt.% Ru/CeO<sub>2-x</sub> at 300 K surface is conducted (Fig. 6). Again as in the case of hydrogen reduced CeO<sub>2</sub> when compared to CeO<sub>2</sub> there is a shift of the product desorption to lower temperatures by about 40 K. While product distribution remain similar, the main difference with ethanol-TPD of non-reduced Ru/CeO<sub>2</sub> is found at high temperature. While CO<sub>2</sub> desorption occurs at 60 K before that of CO, CH<sub>4</sub> desorption now occurs mainly at the high temperature side (740 K). The difference in the desorption profile can be rationalized in terms of the initial surface states where Ru is present as metallic at the beginning of ethanol-TPD of prior H<sub>2</sub>-reduced Ru/CeO<sub>2</sub> and therefore more homogeneously distributed on the surface.

### 3.5. Ethanol steam reforming on 0.5 wt.% Ru/CeO<sub>2</sub>

It is possible to link the observations gained from TPD to real catalytic reactions of ethanol. Ethanol steam reforming (ESR) on Ru/CeO<sub>2</sub> systems, as a function of temperature and gas flow rate, was studied to investigate their effects on the production of hydrogen. The results are shown in Table 2 and Fig. 7. ESR was performed at 573, 673, 773 and 823 K for a fixed inlet liquid flow rate of 10 mL g<sub>Catal</sub><sup>-1</sup> h<sup>-1</sup>. The reaction was allowed to proceed until a steady state condition was reached at each temperature and was tested both ways from 573 to 773 K and vice versa. Each point in the table is the average value of 4–6 injections. The outlet gas flow rate was measured to estimate the overall activity of the reaction. Upon increasing the temperature from 573 to 673 K production of H<sub>2</sub> increases considerably as the steam reforming is an endother-



mic and also because as indicated during TPD the high temperature channel does not start below 650 K. Further increase of temperature above 673 K leads to the decrease of the production of H<sub>2</sub>. While WGS reaction is exothermic and therefore a decrease in its contribution is expected, the continuous reforming of methane should be providing more hydrogen. This has been observed on other systems such as the Pd/CeO<sub>2</sub> and Rh-Pt/CeO<sub>2</sub> catalysts [11,12]. This results show the limitation of the Ru (alone) system when compared to Pd and Pt (separately). One may invoke that Ru at high temperature kinetically accelerates reverse WGS, most likely due to its higher oxidation capacity [42] when compared to Pt and Pd.

#### 4. Conclusions

Temperature programmed desorption of ethanol was compared over CeO<sub>2</sub> and Ru/CeO<sub>2</sub> and complemented by ethanol steam reforming catalytic experiments. Ru metal particles are well dispersed on CeO<sub>2</sub> with a mean particle size of 1.5 nm. Three main conclusions can be extracted from this study. First, the reduced CeO<sub>2</sub> surface is more active for both dehydrogenation and dehydration reactions of ethanol than the non-reduced CeO<sub>2</sub>. Second, the addition of Ru considerably shifted the reaction from these initially observed two products. Instead, products resulting from reforming and WGS reaction became dominant. Third, the CO and CO<sub>2</sub> desorption during TPD track the catalytic reaction for hydrogen production. Increasing the reaction temperature above 750 K resulted in decreasing the hydrogen yield and this might be due to the role of Ru in kinetically accelerating reverse water gas shift reaction.

#### Acknowledgments

J.L. is Serra Húnter Fellow and is grateful to ICREA Academia program and MINECO grant ENE2015-63969.

#### References

- [1] H. Idriss, M. Scott, V. Subramani, Hydrogen and its properties, chapter in handbook on hydrogen energy Hydrogen Production and Purification, vol. 1, Woodhead Publishing, 2014.
- [2] H. Idriss, *Platinum Metals Rev.* 48 (3) (2004) 105–115.
- [3] D.R. Mullins, *Surf. Sci. Rep.* 70 (2015) 42–85.
- [4] J.M. Floyd, *Ind. J. Technol.* 11 (1973) 589.
- [5] J. Scaranto, H. Idriss, *Top. Catal.* 58 (2015), 1443–148.
- [6] A. Trovarelli, *Catal. Rev.* 38 (4) (2016) 439–520.
- [7] R.J. Byron Smith, L. Muruganandam, S.S. Murthy, *Int. J. Chem. React. Eng.* 8 (R4) (2010).
- [8] A. Yee, S. Morrison, H. Idriss, *J. Catal.* 186 (1999) 279–295.
- [9] A. Yee, S.J. Morrison, H. Idriss, *J. Catal.* 191 (2000) 30–45.
- [10] A. Yee, S.J. Morrison, H. Idriss, *Catal. Today* 63 (2000) 327–335.
- [11] P.-Y. Sheng, A. Yee, G.A. Bowmaker, H. Idriss, *J. Catal.* 208 (2002) 393–403.
- [12] H. Idriss, M. Scott, J. Llorca, S.C. Chan, W. Chiu, P.Y. Sheng, A. Yee, M.A. Blackford, S.J. Pas, A.J. Hill, F.M. Alamgir, R. Rettew, C. Petersburg, S. Senanayake, M.A. Barteau, *ChemSusChem* 1 (2008) 905–910.
- [13] P.-Y. Sheng, G.A. Bowmaker, H. Idriss, *Appl. Catal. A* 261 (2004) 171–181.
- [14] P.Y. Sheng, H. Idriss, *J. Vac. Sci. Technol. A* 22 (4) (2004) 1652–1658.
- [15] C. Digne, H. Idriss, A. Kiennemann, Hydrogen production by ethanol reforming over Rh/CeO<sub>2</sub>-ZrO<sub>2</sub> Catalysts, *Catal. Commun.* 3 (2002) 565–571.
- [16] N.J. Divins, I. Angurell, C. Escudero, V. Pérez-Dieste, J. Llorca, *Science* 346 (2014) 620–623.
- [17] M. Baruah, P. Dixit, D. Basarkar, *Renew. Sust. Energy Rev.* 51 (2015) 1345–1353.
- [18] E. Varga, P. Pusztai, L. Ovari, A. Oszko, A. Erdohelyi, C. Papp, H.P. Steinruck, Z. Konya, J. Kiss, *Phys. Chem. Chem. Phys.* 17 (2015) 27154–27166.
- [19] P. Parthasarathy, K.S. Narayanan, *Renew. Energy* 66 (2014) 570–579.
- [20] Z. Wei, J. Sun, Y. Li, A.K. Datye, Y. Wang, *Chem. Soc. Rev.* 41 (2012) 7994–8008.
- [21] J.J. Carroll, K.L. Haug, J.C. Weisshaar, M.R.A. Blomberg, P.E.M. Siegbahn, M. Svensson, *J. Phys. Chem.* 99 (1995) 13955.
- [22] L.M. Martínez, M. Araque, M.A. Centeno, A.C. Roger, *Catal. Today* 242 (2015) 80–90.
- [23] I.A. Carbajal-Ramos, M.F. Gomez, A.M. Condo, S. Bengio, J.J. Andrade-Gamboa, M.C. Abello, F.C. Gennari, *Appl. Catal. B: Environ.* 181 (2016) 58–70.
- [24] E.B. Pereira, N. Homs, S. Martí, J.L.G. Fierro, P.R. de la Piscina, *J. Catal.* 257 (2008) 206–214.
- [25] C. de Leitenburg, A. Trovarelli, J. Käspar, *J. Catal.* 166 (1997) 98–107.
- [26] J. Lin, L. Zhang, Z. Wang, J. Ni, R. Wang, K. Wei, *J. Mol. Catal. A: Chem.* 366 (2013) 375–379.
- [27] W. Xu, R. Si, S.D. Senanayake, J. Llorca, H. Idriss, D. Stacchiola, J.C. Hanson, J.A. Rodriguez, *J. Catal.* 291 (2012) 117–126.
- [28] H. Idriss, C. Digne, J.P. Hindermann, A. Kiennemann, M.A. Barteau, *J. Catal.* 155 (1995) 219–237.
- [29] S. Banerjee, *New J. Chem.* 39 (2015) 5350–5353.
- [30] W. Kenji, H. Saburo, I. Masashi, *Catal. Surv. Asia* 15 (2011) 1–11.
- [31] M.A. Nadeem, G.I.N. Waterhouse, H. Idriss, *Catal. Struct. React.* 1 (2) (2015) 61–70.
- [32] H. Idriss, K.S. Kim, M.A. Barteau, *J. Catal.* 139 (1993) 119–133.
- [33] J. Muir, H. Idriss, *Chem. Phys. Lett.* 572 (2013) 125–129.
- [34] G. Busca, J. Lamotte, J.-C. Lavalley, V. Lorenzelli, *J. Am. Chem. Soc.* 109 (1987) 5197–5202.
- [35] J.N. Muir, Y.M. Choi, H. Idriss, *Phys. Chem. Chem. Phys.* 14 (2012) 11910–11919.
- [36] Y.-M. Choi, M. Scott, H. Idriss, *Phys. Chem. Chem. Phys.* 16 (41) (2014) 22588–22599.
- [37] H. Idriss, M.A. Barteau, *Adv. Catalysis* 45 (2000) 261–331.
- [38] H. Idriss, in: G. Ertl, H. Knözinger, F. Schüth, J. Weitkamp (Eds.), *Handbook of Heterogeneous Catalysis*, vol. 3, 2nd edition, Wiley-VCH, 2008, pp. 1338–1352 (Chapter 4.6, ISBN 978-3-527-31241-2).
- [39] A. Bruix, A. Migani, G.N. Vayssilov, K.M. Neyman, J. Libuda, F. Illas, *Phys. Chem. Chem. Phys.* 3 (2011) 11384–11392.
- [40] G.N. Vayssilov, Y. Lykhach, A. Migani, T. Staudt, G.P. Petrova, N. Tsud, T. Skála, A. Bruix, F. Illas, K.C. Prince, V.R. Matoliñ, K.M. Neyman, J. Libuda, *Nat. Mater.* 10 (2011) 310–315.
- [41] K. Ševčíková, V. Nežas, M. Vorokhta, S. Haviar, V. Matolín, I. Matolínová, I. Mašek Piš, M. Kobata, T. Nagata, Y. Matsushita, H. Yoshikawa, *Mater. Res. Bull.* 67 (2015) 5–13.
- [42] D. Strmcnik, M. Uchimura, C. Wang, R. Subbaraman, N. Danilovic, D. van der Vliet, A.P. Paulikas, V.R. Stamenkovic, N.M. Markovic, *Nat. Chem.* 5 (2013) 300–306.